The Nanoscale Implications of a Molecular Gas Beam during Electron Beam Induced Deposition

Robert Winkler,[†] Jason Fowlkes,[‡] Aleksandra Szkudlarek,[§] Ivo Utke,[§] Philip D. Rack,[‡,||] and Harald Plank*[,†,⊥]

[†]Center for Electron Microscopy, Steyrergasse 17, 8010 Graz, Austria

[‡]Center for Nanophase Materials Sciences, Oak Ridge National Laboratory, Oak Ridge, Tennessee 37831, United States

[§]EMPA, Swiss Federal Laboratories for Materials Science and Technology, Laboratory for Mechanics of Materials and Nanostructures, Feuerwerkerstrasse 39, 3602 Thun, Switzerland

[||]Department of Materials Science and Engineering, University of Tennessee, Knoxville, Tennessee 37996, United States

[⊥]Institute for Electron Microscopy and Nanoanalysis, Graz University of Technology, 8010 Graz, Austria

Ⓢ *Supporting Information*

ABSTRACT: The gas flux direction in focused electron beam induced processes can strongly destabilize the morphology on the nanometer scale. We demonstrate how pattern parameters such as position relative to the gas nozzle, axial rotation, scanning direction, and patterning sequence result in different growth modes for identical structures. This is mainly caused by nanoscale geometric shadowing, particularly when shadowing distances are comparable to surface diffusion lengths of $(CH_3)_3$-Pt-$CpCH_3$ adsorbates. Furthermore, two different adsorbate replenishment mechanisms exist and are governed by either surface diffusion or directional gas flux adsorption. The experimental study is complemented by calculations and dynamic growth simulations which successfully emulate the observed morphology instabilities and support the proposed growth model.

molecular gas flux direction

balanced precursor regime   *directional gas flux effects*

KEYWORDS: *focused electron beam induced deposition, nanofabrication, platinum, simulation*
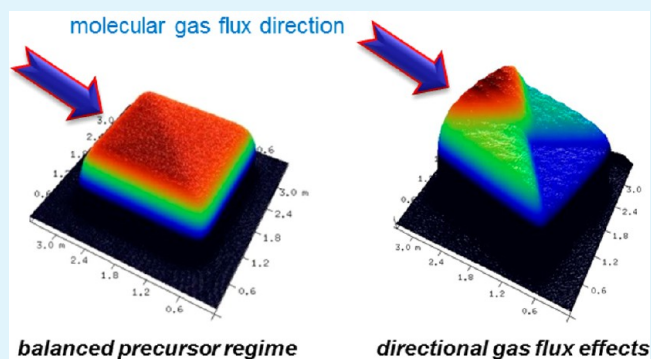
■ INTRODUCTION

Electron beam induced deposition (EBID) provides a unique method to direct write functional 3D nanostructures[1−3] on almost any substrate material or shape. EBID mostly uses gaseous precursors which are injected into the vacuum chamber via a localized gas injection system (GIS) close to the point of deposition. Alternative strategies implementing liquid phase precursors/media have also recently emerged.[4] Gaseous precursors consist mainly of organometallic precursor molecules[5] which adsorb and diffuse on the surface and eventually desorb after a residence time if not consumed/decomposed by the electron beam.[1,3,6−10] The deposition is based on electron beam induced decomposition which dissociates the precursor molecules into immobilized functional condensates and volatile fragments which are pumped away from the chamber.[1−3,11] Thus, very small (3D) structures can be fabricated on even nonflat surfaces with spatial resolutions below 10 nm.[12] In recent years, an increasing number of applications have been demonstrated, ranging from passive applications such as nano optics,[13] lithography-mask repair,[14] nanolithography,[15,16] vapor−liquid−solid nanowire growth templating,[17] atomic-layer-deposition seeding,[18] advanced scanning probe micros-copy probes,[19] and diodes[20] toward active devices such as

magnetic storage, sensing and logic applications,[21] nanoscale strain sensors,[22,23] and gas sensors.[24] Most of the applications have two main performance demands: (1) high morphological control to allow reproducible fabrication of required geometries and (2) defined chemistry for proper functionality. Both of these requirements depend strongly on the precursor working regime during deposition which can be described by the balance between dissociating electrons and available precursor adsorbates[1,3,9,11,25,26] with two extremes: (i) more adsorbates than electrons, which is typically referred to as reaction rate limited (RRL), and (ii) more electrons than adsorbates, which is referred to as mass transport limited (MTL). It is known that a regime change not only changes the volumetric growth rate and resolution[1,9,11,27] but also the chemistry/composition.[28−30] Hence, control of the working regime is critical to define and reproduce the morphology and functionality. Regarding the chemistry, several ex and in situ strategies have been developed in order to modify the functionality, such as parameter optimization,[7,28] heated substrates,[31,32] reactive gases,[33,34] in

situ laser assist,[35,36] thermal postgrowth annealing,[37,38] post-growth e-beam curing,[39] and other combined processes.[38,40,41] On the basis of this progress in functional material tuning, advanced industrial applications are a step closer to reality. However, the final device performance depends strongly on both the shape fidelity and chemistry, which is therefore a primary gateway for potential applications.

In this study, we focus on the influence of the inhomogeneous molecular gas flux on final deposit shapes and the dependence on position, orientation, and electron scanning sequences used during electron beam patterning. It is demonstrated that the inhomogeneous gas flux including shadowing effects[42−45] leads to a directional replenishment component which can destabilize the growth mode. Finally, counterstrategies via beam current and pixel dwell time variations are presented which reveal the existence of two different types of MTL conditions dominated by (1) the gas flux and (2) surface diffusion. The study is complemented by calculations and finite difference growth simulations revealing excellent agreement with the experimental findings.

■ EXPERIMENTS

Gas Flux Vector. The experimental setup of our system uses an FEI gas injection system (GIS) with an angle of 52° with respect to the sample surface. The electron beam scan rotation was used to align the GIS main axis (along the needle) in the imaging window (see Figure 1a). All deposits were synthesized at a distance of 40 μm with respect
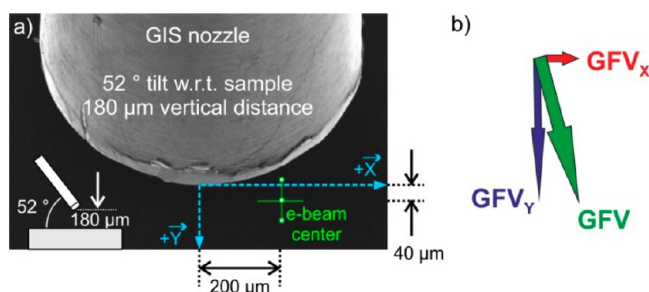

Figure 1. (a) SEM image of the gas injection system (GIS) relative to the center of the electron beam (green cross) at a distance of 200 and 40 μm for X and Y, respectively. The inset in the bottom left shows the vertical distance and the GIS angle. The blue dashed arrows define X and Y axes used for the discussion. (b) Gas flux vector (GFV) derived from simulations and experiments (see main text) including its individual X and Y components GFV_X and GFV_Y, respectively, for the given setup in part a.

to the GIS (defined as the Y direction) and 200 μm from the GIS main axis (defined as the X direction), as shown by the green cross in Figure 1a. Please note that the off-axis alignment of 200 μm was deliberately chosen to demonstrate the effects of the gas flux direction. Friedli et al. showed that, as a consequence of the finite nozzle diameter, sample surface distance, and tilted GIS arrangement, the molecular adsorption rate is site-specific due to the spatially varying gas flux GF(x, y, z).[42,45,46] In the following, we reduced this expression to GF(x, y) due to the flat substrates and comparably flat deposits less than 200 nm thick. The gas flux simulator (GFS) by Friedli and Utke et al.[46] was used to simulate the relative flux ratio J/J_{TOT}. The GFS results were compared to quasi 1D nanopillar experiments where surface diffusion from the substrate is minimized and the growth rates limited by local gas flux adsorption (shown in Supplement 1, Supporting Information). Importantly, the main gas flux vector (GFV) with respect to the X axis was determined to be ∼72 and ∼75° by simulations and experiments, respectively (shown in Supplement 1, Supporting Information). For

convenience, X and Y directional components, GFV_X and GFV_Y, of the main GFV are used, as shown in Figure 1b.

Scan Directions. First, experiments with 3D pads were performed with high beam currents (1600 pA) and long DTs (1000 μs) via single pass patterning (2 × 2 μm^2 footprint, 13 nm point pitch). These parameters were chosen to increase precursor depletion in the beam area and its proximity as observed in previous studies which revealed reduced coverage in a radius of about 60 nm for comparable conditions and low DTs.[47] The reduced coverage is due to adsorbate consumption during long beam pulses with high electron flux. This is experimentally demonstrated via VGR experiments for increasing DTs which show an initial decay followed by a constant value (see Supplement 2, Supporting Information, and refs 1, 3, 7, 27, and 28). The nonzero steady state volume growth rate (VGR) reflects the constant gas flux replenishment which is independent of the DTs used.[47] Thus, to simplify our interpretation and directly infer the gas flux dependent growth, we performed experiments at high currents together with high DTs (see also Supplement 2, Supporting Information).

Initially, serpentine (SP) scans were used, as schematically shown in Figure 2a. We define the scanning direction along consecutive patterning points as the fast scan axis (FSA), while the slow scan axis (SSA) is the direction perpendicular to the FSA, as indicated by solid arrows in Figure 2a. Note the alignment of the gas flux vector GFV and its X and Y components (GFV_X, GFV_Y) relative to the scan axes. In order to elucidate the effect of the SSA with respect to the GFV, the serpentine patterns were rotated, as indicated in the four segments in Figure 2a (denoted as SP1, SP2, SP3, and SP4). AFM measurements reveal flat structures for all these patterning directions (representatively shown in Figure 2b) and enable quantitative volume analyses. The solid red bars in Figure 2c show their relative VGRs for all four orientations, revealing variations up to 35%. Comparing the different orientations, several details emerge: (1) the highest VGRs occur when the SSA vector points toward the strongest gas flux component GFV_Y (SP3), and (2) patterning away from the GFV_Y direction gives the lowest VGRs (SP1). A similar trend is observed with respect to the weaker gas flux component GFV_X. Further experiments with reversed FSA directions were conducted, revealing identical height distributions (see Supplement 3, Supporting Information). Thus, it was concluded that the relative orientation of patterning direction and gas flux vector GFV can influence the growth.

Special Patterning Strategies. In order to visualize gas flux vector effects within one single pad, a spiral-out (SO) patterning strategy was introduced which conveniently scans consecutively in different directions relative to the gas flux vector GFV. Figure 3a shows a 3D AFM height image of a deposit fabricated by an SO strategy (bottom left) with a single pass (identical parameters relative to the previous section). Although each patterning point was exposed to the electron beam once, the deposit shows a terraced structure in contrast to the widely flat deposits achieved with the serpentine patterns, as shown in Figure 2b.

Besides the strong height difference of the front (1) and back segments (3), slightly different heights are also found for the lateral segments (2 and 4) (higher and lower, respectively). To mimic the experiments, a finite difference algorithm was written and executed to estimate the dynamic surface coverage and EBID deposit heights using identical SO patterning conditions as those used for Figure 3a (details can be found in the Methodology section and in Supplement 4, Supporting Information). To simplify, only the y-component of the gas flux vector GFV was simulated perpendicular to the deposit front edge. Figure 3b shows the simulated deposit heights, which is very similar to what was observed experimentally (Figure 3a). Figure 3c reveals that the highest adsorbate surface coverage is realized on the front side with respect to the gas flux vector GFV (dark parts), while the lowest coverage exists on the deposit back side (yellow regions). Interestingly, surface coverage "crevices" are observed at the boundaries of the four segments, as noted in Figure 3c. A detailed look at the temporal coverage evolution reveals furthermore that the height difference between the lateral segments (2, 4) and the back segment (3) starts to increase with a larger spiral diameter (see the
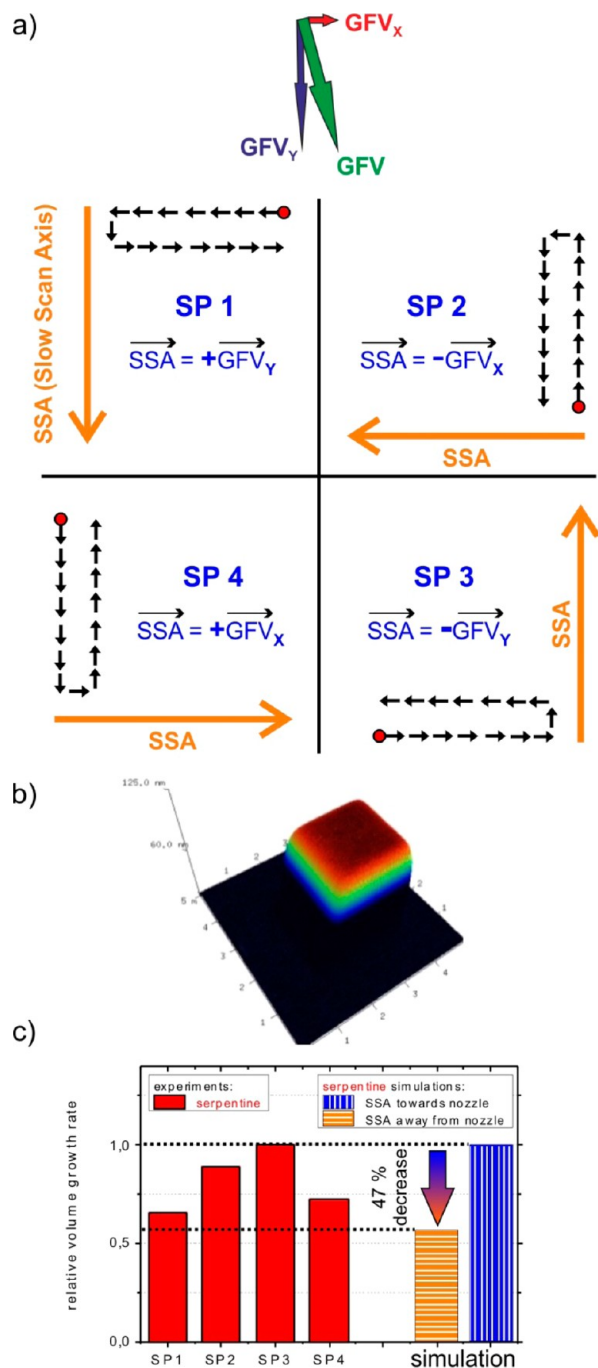
Figure 2. Variable serpentine patterns: (a) basic patterning strategy including the slow scan axis vector SSA. The four segments show the SSA orientation for SP1, SP2, SP3, and SP4 relative to the gas flux vector GFV (see Figure 1) and its X and Y components (GFV_X, GFV_X). (b) Representative AFM height image of a deposit fabricated via the serpentine pattern. (c) Relative VGRs for different pattern orientations defined in part a for serpentine strategies (solid bars, highest VGR used as reference value). Simulation results are shown by the two bars at the right with SSA orientation toward (vertical stripes and analogous to SP3) and away from the gas flux (horizontal stripes and analogous to SP1), revealing 47% decrease in VGR which is in good agreement with the experimental trend (see dotted lines).
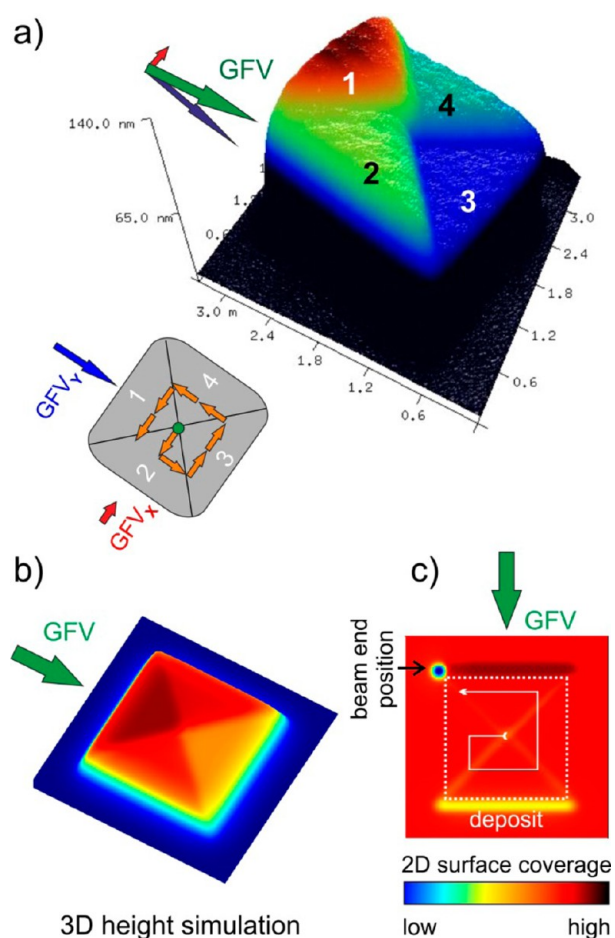
Figure 3. (a) AFM height image of a spiral-out deposit fabricated with a single pass. The relative orientation of the gas flux vector and its components are shown in the top left. The scanning strategy is indicated in the bottom left together with the individual gas flux components GFV_X and GFV_Y. (b) Simulation results using the same process parameters as those for the deposit in part a, however, with only the GFV_y component oriented perpendicular to the deposit front (see green arrow). Due to the missing GFV_X component, segments 2 and 4 have the same simulated height. (c) Simulated surface coverage after one complete spiral-out scan. The lowest coverage is observed on the back segment, and the highest, on the front segment (facing the GFV). Please note the small coverage crevices behind the segments (slightly brighter). The patterning box frame (dotted line) and the scanning strategy used (solid arrows) are also indicated.

beam travels clockwise and showed identical results (see Supplement 5, Supporting Information).

Pattern Rotation. As discussed in the previous section, the SO deposit shows also a lateral asymmetry in height (segments 2 and 4 in Figure 3a), which was not found for the simulations. The symmetry observed in the simulations is due to the small X component of the gas flux vector which was ignored. In order to investigate the relation between the GFV_X component and the observed asymmetry, the SO patterns were experimentally rotated in 15° increments. As observed in Figure 4, the height distribution for four segments varies depending on the orientation relative to the GFV and the height variations scale with the magnitude of GFV_X and GFV_Y. Interestingly, at 30° rotation, the GFV is parallel with the square diagonal and the front two segments have equivalent heights which are thicker than the back two segments which also have equivalent thickness. At 75°, the gas flux vector GFV is perpendicular to one of the square edges (see Supplement 1, Supporting Information). Similar to the simulation, in this case, the side segments are of equivalent thickness and the front and back have

movie in the Supporting Information) as a consequence of the triangularly shaped front segment. Note that the spiral-out patterns were also investigated in the opposite scanning directions where the
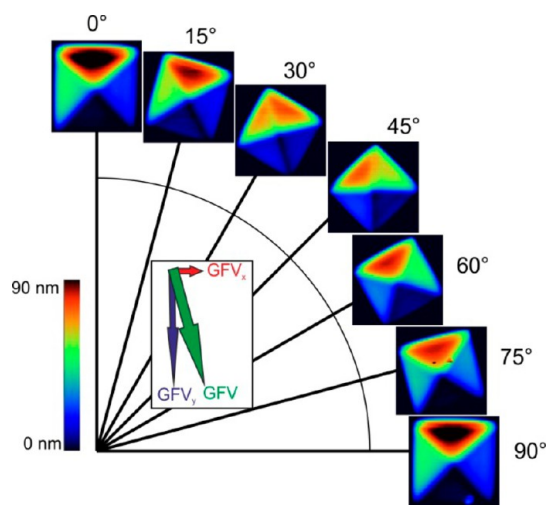
Figure 4. Pattern rotation for spiral-out patterning (counterclockwise) using the same electron beam parameters used in Figure 3. The gas flux vector is shown relative to the pattern orientation.

the largest thickness variation. The relative magnitudes of the GFV components clearly and systematically affect each segment thickness and illustrate the influence it has on the growth modes.

Separation of Gas Flux and Diffusive Replenishment. To separate between gas flux and surface diffusion related replenishment mechanisms, growth experiments without the gas flux were performed. Initially, the GIS system was opened for 3 min to achieve coverage equilibrium at the surface. Then, the GIS valve was closed and retracted before electron beam patterning was started (within less than

3 s). Note that this strategy eliminates the directed gas flux adsorption, while homogeneous precursor adsorption from the chamber volume still occurs as the monitored chamber pressure decays on a larger time scale than the patterning time. The results for SO patterns with identical electron beam parameters revealing thin (sub 5 nm) and flat deposits (see Supplement 6, Supporting Information) without any terraced segments compared to gas flux assisted deposition are shown in Figure 3a. However, even for such high dwell times, the pads are laterally symmetric. To investigate the influence of diffusion related replenishment from the substrate via simulations, the spiral-out experiments summarized in Figure 3 were repeated with a very small diffusion coefficient of 1×10^{-11} cm^2 s^{-1} with an associated diffusion length of less than 0.4 Å. The simulations reveal practically identical results in terms of morphological shapes, absolute heights, temporal behavior, and surface coverage (see Supplement 7, Supporting Information). Together with the GIS-off experiments, it can therefore be concluded that the directed gas flux is responsible for the asymmetrically terraced morphology (Figures 3a and 4). Furthermore, it shows that the surface coverage is widely constant in the deposition area, which is in agreement with the initial 1-D pillar growths (see Supplement 1, Supporting Information).

Beam Current Variation. In order to investigate the influence of the precursor working regime on final morphologies, the electron beam current was varied from 6300 to 5 pA (constant beam energy), while single pass SO patterning was used at a constant dwell time of 1000 μs (decreasing total dose). As shown in the AFM height images in Figure 5, decreasing beam currents lead to stabilized morphologies. The flatter structures emerge due to less gas depletion at lower currents. As a quantitative measure of the decreasing terrace formation, the relative height ratio between the lowest (3) and highest (1) segments is plotted vs the beam current in the center of Figure 5. As can be seen both for highest and lowest currents, the relative height
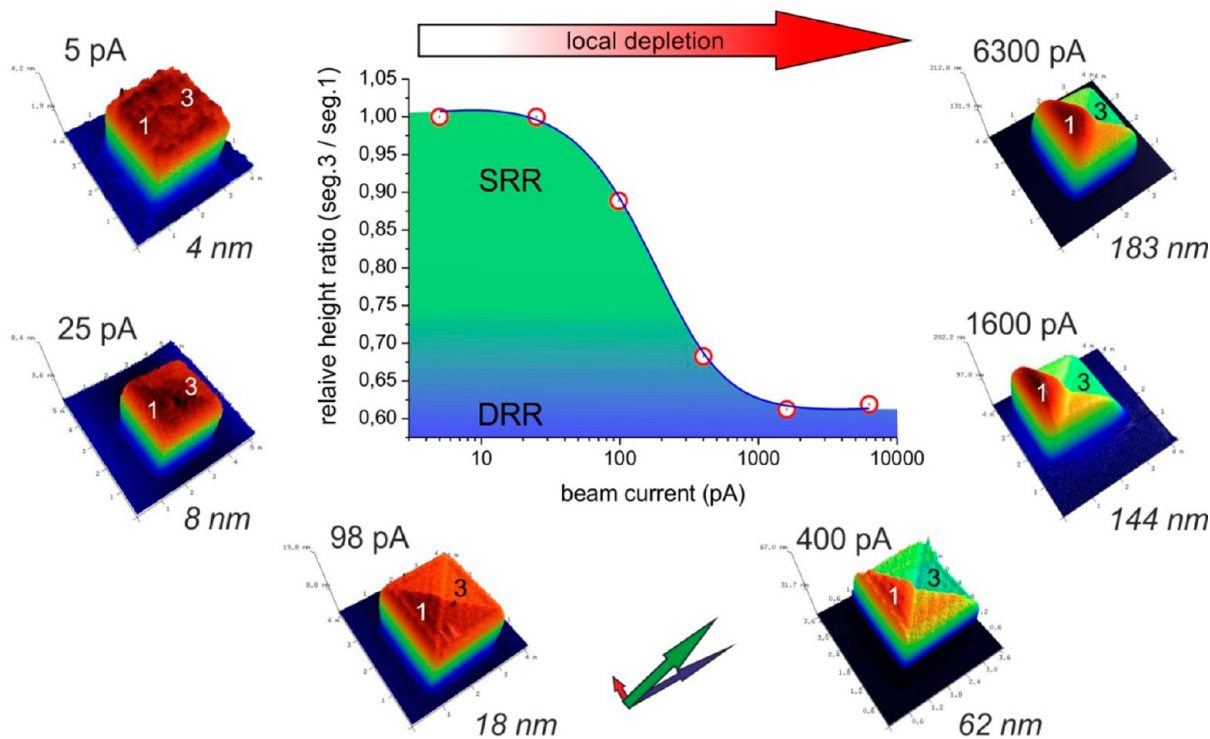

Figure 5. Beam current variation using spiral-out strategies for identical patterning conditions of 5 keV, 13 nm point pitch and 1000 μs pixel exposure via single pass patterning (2 × 2 μm^2 footprint), leading to increasingly flatter structures at lower current. The correctly oriented GFV and its components are also indicated together with the maximum deposit heights (segment 1). The relative height ratio between back and front segments versus beam current (central graph) is a qualitative measure for the surface coverage. For the highest currents, deposit related replenishment (DRR) dominates, while decreasing currents reveal the transition to predominant surface related replenishment (SRR) due to lower depletion and incremental growth heights.
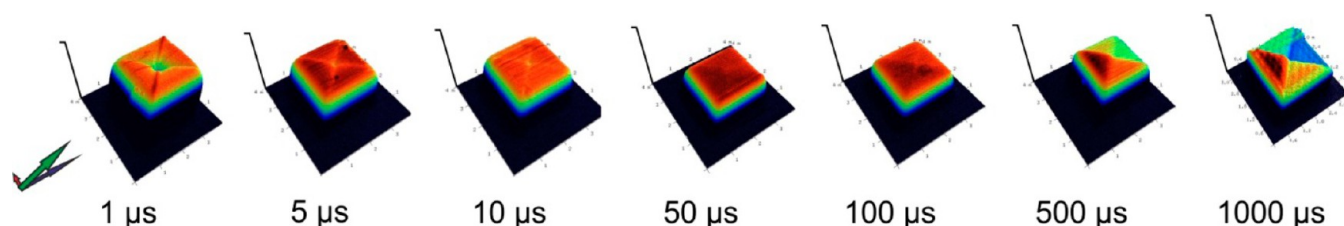
2990

dx.doi.org/10.1021/am405591d | ACS Appl. Mater. Interfaces 2014, 6, 2987–2995

Figure 6. Dwell time variation using spiral-out strategies with adapted patterning loop numbers to keep the total exposure time constant. Color settings are adapted to clearly reveal surface variations. All deposits have the same footprint of 2×2 μm^2, and all vertical scale bars are 200 nm.

difference saturates, which indicates widely constant but very different regime conditions, as will be discussed later.

Pixel Dwell Time Variation. As an alternative to the previously discussed beam current variation, the pixel dwell time was also used to control the local precursor regime. Therefore, SO experiments were conducted with varying pixel dwell times ranging from 1000 to 1 μs, while the number of patterning loops was adapted to maintain the total exposure time (and thus electron dose). Such a DT sweep for 1600 pA is shown in Figure 6 by 3D AFM images which reveal that decreasing dwell times lead to flatter deposits. For very short dwell times of 10 μs and less, additional features appear in terms of a diagonal trench and an even deeper central indent (see the 1 μs deposit in Figure 6).

To correlate the process parameters with the unstable morphology, AFM based height histograms were taken from all deposits. For defined shapes, the histogram shows very sharp peaks, as shown for the 50 μs deposit in Figure 7a (center). For the terraced 1000 μs deposit, as shown in Figure 3a, the histogram shows four distinct peaks, as can be seen in Figure 7a on the right. The trench and indent formation for the 1 μs deposit is accompanied by an asymmetric peak, as shown in Figure 7a on the left. When measuring the base widths of these histogram peaks and plotting vs dwell times for different currents, one obtains the diagram shown in Figure 7b. As can be seen, the morphology destabilizes for high and low dwell times, however, for very different reasons as will be discussed below.

DISCUSSION

As discussed and summarized in Figure 2, the VGR was highest when patterning was performed toward gas flux vector components GFV_X (SP2) and GFV_Y (SP3) where new deposition areas are efficiently replenished by the gas flux. In contrast, when patterning away from the gas flux components, deposition occurs in the geometric shadow of the deposit[42−45] which inhibits replenishment, as schematically shown in Figure 8a. For the given geometry, we can estimate the most beneficial geometric shadowing radius Δr_S on the back side of the deposit as a function of the deposit height h to >20% ($\Delta r_S = 0.2*h$) assuming straight molecule trajectories between the GIS and substrate/deposit. This suggests a geometric shadowing radius Δr_S of a minimum 20−30 nm for the deposits SP1−SP4 (see Figure 2). On the basis of a diffusion constant D_0 of 6.5×10^{-9} to 8.5×10^{-10} cm$^2 \cdot$s^{-1} and a typical residence time τ of 60−100 μs, this results in a radial diffusion length $\langle r \rangle$ between 2 and 25 nm according to $\langle r \rangle = (4*D_0*\tau)^{1/2}$ assuming 2D random surface diffusion (details about D_0 and τ can be found in Supplement 8, Supporting Information).[1,3,7,9] A shadowing radius of at least 20 nm suggests that the back side of the deposits cannot be efficiently replenished via diffusion of molecules that adsorb outside the shadowing radius because they desorb before reaching the deposit back side. A certain fraction of these desorbing molecules, however, are assumed to readsorb on the deposit back side and contribute to the precursor population. Both replenishment mechanisms, diffusion and readsorption, are further denoted as *substrate related*
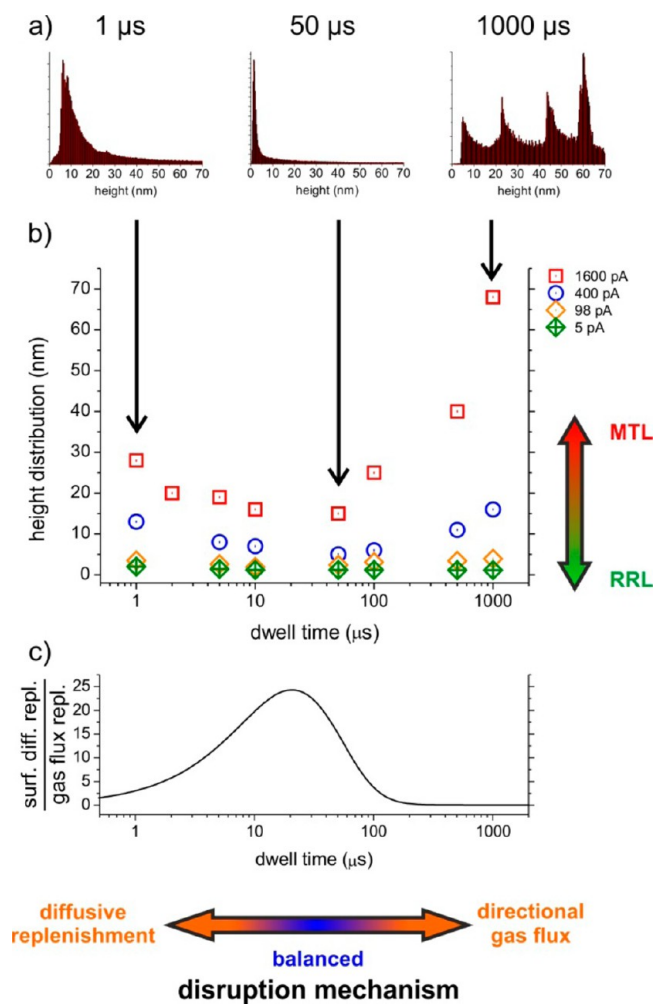

Figure 7. (a) Comparison of AFM pixel height histograms from experimental deposits for selected dwell times. (b) Summary of the histogram peak base widths as a function of dwell time and beam current. (c) Calculated ratio of diffusive replenishment vs gas flux adsorption replenishment at the center of the electron beam as a function of the same dwell time range as for part b with a current of 1600 pA (compare to red squares in part b).

replenishment (SRR) throughout the manuscript. On the other hand, for molecules which adsorb on top of the deposit, close to the growing front, it is possible to diffuse "downwards" and contribute to the growth which we denote as *deposit related replenishment* (DRR). Note that the estimations given above are based on the 20% criterion for the shadowing radius related to the most beneficial angle, while a majority of trajectories show higher shadow radii illustrated by green and red lines in Figure 8a, respectively. On the basis of these estimations, the observed VGR dependency on the SSA orientation with respect to GFV
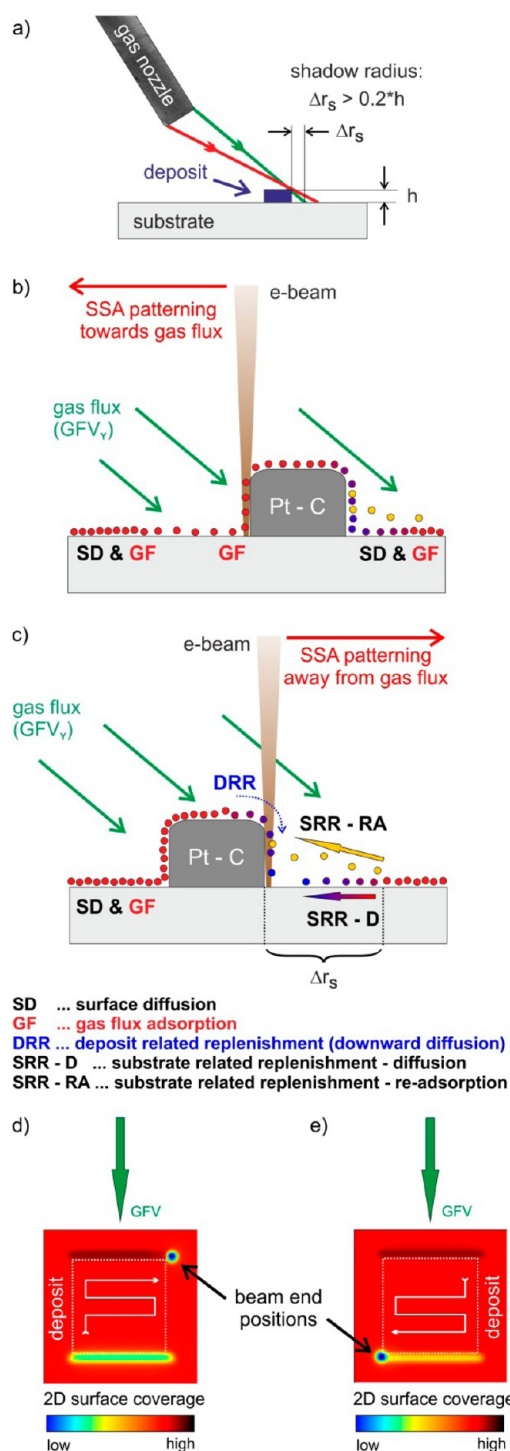
2991

dx.doi.org/10.1021/am405591d | *ACS Appl. Mater. Interfaces* 2014, 6, 2987−2995

Figure 8. (a) Schematic of geometrical shadowing as a consequence of the GIS tilt angle and its distance to deposit. The suggested coverage and replenishment mechanism during patterning toward and away from the gas flux are shown in side view schemes in parts b and c, respectively. The 2D plots in parts d and e show simulations of the surface coverage at the termination of a beam dwell cycle from a top view, revealing higher and lower precursor population on the deposit front and back side, respectively. For as explanation, please consult the main text.

can be interpreted as follows: when patterning with the SSA toward the GFV_Y gas flux component (SP3 in Figure 2), as illustrated in Figure 8b, the front side of the growing deposits gets directly replenished by the gas flux, while substrate related

replenishment is reduced as a result of the high dwell times used. To further investigate this hypothesis, finite difference simulations were performed for the purpose of estimating the dynamic surface coverage and deposit heights (details can be found in the Methodology section and in Supplement 4, Supporting Information) using a similar geometrical setup as described in the "Scan Directions" section and shown in Figure 2. The surface coverage distributions are shown by 2D top view plots in Figure 8d and 8e and reveal an increased molecular coverage on the front side due to direct gas flux replenishment (dark areas) and relatively low coverage at the back side as the consequence of geometrical shadowing (yellow areas). In contrast, when patterning is performed away from the GFV_Y component (SP1), as shown in Figure 8c, new deposition takes place in the geometrical shadow region where direct gas flux replenishment is restricted to the topmost edge areas of the structures. Due to the nonzero VGR, deposit related replenishment via downward diffusion is assumed to predominantly populate the evolving deposition front, as indicated by the DRR labeled arrow in Figure 8c. Substrate related replenishment (SRR) is assumed to be reduced as the precursor molecules tend to desorb before they diffuse through the shadowing radius Δr_S toward the growing deposit (see SRR-D path in Figure 8c), while readsorption can slightly contribute to the growth (SRR-RA path). Complementary surface coverage simulations (Figure 8e) reveal again that deposition takes place in areas of lower surface coverage (yellow areas), which explains the lower VGRs when patterning away from the gas flux. Quantitative simulation analyses of the VGRs suggest a VGR decay of 47% when patterning away from the gas flux (Figure 2c). A similar argument holds for SP2 and SP4 patterns relative to the GFV_X component. The fact that $GFV_y > GFV_x$ explains why higher VGRs are found for SP3 (toward Y) compared to SP2 (toward X), as summarized in Figure 2c. From these experiments, it can be concluded that a *directional gas flux replenishment component* is caused by (1) the GIS position with respect to the deposit (absolute X direction) together with (2) a geometric shadowing effect which depends on the absolute Y distance and the GIS tilt angle, as previously described by Friedli et al.[42−45]

The spiral-out (SO) patterning strategy allows one to visualize both directional gas flux replenishment components with one pattern. The terraced deposit shown in Figure 3a can be explained by directional gas flux effects: during patterning in segment 1, the strongest gas flux component GFV_Y replenishes the growing deposit front. Subsequently, during growth within segment 2, the replenishment situation is determined by the weaker gas flux component GFV_X. The decreased VGR results in a lower segment height, which furthermore induces geometrical shadowing, as suggested by the simulations (see surface coverage plot in Figure 3c). Both effects together explain the decreasing height for segment 2 in Figure 3a and b. When moving into segment 3, geometrical shadowing further decreases the replenishment of the growing back side (Figure 8c), leading to the lowest segment height which is also in agreement with the coverage simulations shown in Figure 8e. Finally, segment 4 evolves similarly to segment 2 but with the experimental difference that the gas flux component GFV_X is reduced and thus is the slightly reduced height compared to segment 2 (see Figure 3a). Finally, the experiments with a retracted and closed GIS system demonstrate that the destabilized morphology for SO strategies can be attributed

to the gas flux, while surface diffusion effects from surrounding areas are of minor relevance.

On the basis of the previous discussion, it follows that reducing the local depletion should decrease the influence of directional gas flux components. This can be done by two different approaches: (1) reducing the beam current and (2) decreasing the pixel dwell time. As shown in Figure 5, the highest beam currents have a saturated height ratio between front and back segments (central graph), which indicates constant replenishment conditions. Considering the estimated minimum shadowing radius $\Delta r_S = 45$ nm (6300 pA deposit), substrate related replenishment via diffusion and readsorption is assumed to be negligible. This explains the lower plateau for the highest currents where downward diffusion of molecules (DRR) is assumed to be the dominant replenishment mechanism (blue areas in Figure 5). As the beam current decreases, the back side replenishment increases via SRR (Figure 8c) due to (1) reduced local depletion (and a shift toward RRL-like conditions) and (2) reduced geometric shadowing as a result of decreased growth height. Once the surface coverage equilibrates over the entire deposit, the height ratio between segments 3 and 1 approaches 1 (upper plateau in Figure 5) and the directional gas flux components have no further implication. Alternatively, the pixel dwell times can be reduced while the number of patterning loops is increased accordingly, which should again lead to reduced local depletion. As shown in Figure 6 for SO strategies (constant beam current), the deposits get flatter for decreasing pixel dwell times for the same reasons as for decreasing beam currents. The central indent and the diagonal trenches, observed for lowest dwell times, are a result of the SO patterning strategy. Both effects indicate locally higher depletion due to more stationary beam movements at the center (starting point) and at directional changes at the diagonals (>25 nm FWHM beam diameter compared to 13 nm point pitch). To allow the assignment of indent/trench formation to insufficient surface diffusion, SO patterns have been fabricated for shortest dwell times with a retracted and closed GIS, leading to the same central indents and diagonal trenches (see Supplement 6, Supporting Information), which excludes the directional gas flux as the origin of these features. Taking these mechanisms into account, the morphological destabilization for very low and very high pixel dwell times, summarized in Figure 7b, can both be understood as a consequence of a regime shift toward more MTL-like conditions, however, due to different reasons: while the directional gas flux dominates for high dwell times (directional replenishment and shadowing), insufficient diffusive replenishment leads to the observed instabilities for low dwell times (see horizontal arrow in Figure 7c). When the beam current is reduced, the deposits become more flat (see Figure 5b) as a consequence of a regime shift toward more RRL conditions (vertical arrow in Figure 7b) where the number of adsorbates density is comparable to the electron flux.

To investigate this situation in more detail, numerical calculations of the local surface replenishment were conducted by considering surface related diffusion and gas flux adsorption individually. The results for the 1600 pA beam current are shown in Figure 7c (calculation details can be found in Supplement 8, Supporting Information). Starting from the longest dwell times, it can be seen that the surface diffusion related replenishment is increasing for decreasing dwell times while the impinging gas flux is constant. The highest surface diffusive replenishment coincides with flat deposits for DTs between 10 and 100 μs (see Figure 6). This increasing SDR contribution results in the more balanced situation between locally available precursor molecules and electrons, leading to widely flat surface structures. Further decreased dwell times lead to reduced depletion and thus to smaller concentration gradients, resulting in lower diffusive replenishment contributions, as shown in Figure 7c.

CONCLUSIONS

The study demonstrates how the inhomogeneous molecular gas flux which results from a standard gas injection system can significantly influence the growth modes during focused electron beam induced deposition processes. We demonstrate that the gas flux vector and the patterning strategy in terms of the absolute arrangement, axial rotation, point sequence, and patterning direction during EBID can significantly change the resultant growth rate and can give rise to interesting growth instabilities and morphologies. In the context of applications, it should be kept in mind that spatially varying precursor working regimes might entail different deposit compositions.[28] This, in turn, implies undefined and inhomogeneously distributed deposit functionality which is highly unwanted for potential applications. Together with destabilized morphologies, the study points out the importance of a careful adaption of geometrical setup, beam parameters, and patterning strategies to exploit the full potential of EBID on its way to real applications. Considering the main advantages of this method as a direct-write 3D nanostructuring tool, understanding these interactions is critical to enhancing resolution and maintaining high-fidelity 3D nanopatterns.

METHODOLOGY

Deposition experiments were performed with an FEI NOVA 200 (FEI, The Netherlands) dual beam system equipped with an FEI gas injection system (GIS) for Pt−C deposition using a MeCpPt(IV)Me$_3$ precursor. The GIS has an inner and outer diameter of 500 and 830 μm, respectively, and in this study, the distance between the lower edge of the GIS needle and the sample was set at 180 ± 10 μm. 15 × 15 mm^2 Si samples with 3 nm of SiO$_2$ were used and prepared in a laminar flow box for experiments. After immediate transfer of the samples to the dual beam microscope chamber, a background pressure of at least 9×10^{-6} mbar was established before any experiment was conducted. The precursor was preheated to 45 °C for at least 30 min. Beam focusing and optimization were performed on different areas than the final experiments in order to prevent any cross-contamination. Prior to any deposition, the GIS nozzle was opened for at least 3 min to provide a stable equilibrium between adsorption and desorption. The chamber pressure typically increased to a stable value of 3×10^{-5} mbar during deposition. Lateral positioning was always done in such a way that the GIS nozzle opening is not intersected with substrate edges which could disturb the molecular flux. The electron column sample distance was 5 mm for all experiments. Stage movements to defined areas have been performed with a blanked e-beam followed by deposition and an additional stage movement away from the actual deposition area. All patterns used stream files which have been generated via Matlab (release 2010b, MathWorks, U.S.) and double checked for errors in the point sequence. After successful deposition, the structures were characterized via atomic force microscopy (AFM) performed with a Dimension 3100 microscope (Bruker AXS, U.S.) operated with a Nanoscope IVa controller and equipped with an XYZ Hybrid scan head using an Olympus OMCL TS-160/TS-240 cantilever in tapping mode. Analyses were performed using NanoScope Analysis software (v1.4, Bruker AXS, U.S.). A detailed description of the finite difference simulation is given in Supplement 4 (Supporting Information).

2993

dx.doi.org/10.1021/am405591d | ACS Appl. Mater. Interfaces 2014, 6, 2987−2995

■ ASSOCIATED CONTENT

S Supporting Information

Detailed comparisons between gas flux simulations and experiments to derive the gas flux vector for the technical setup used; dwell time dependent volume growth rate investigations to demonstrate precursor regime shifts toward MTL-like conditions for high dwell times for high beam currents; mirrored serpentine strategies to investigate VGR variation for different patterning directions; detailed description of finite difference simulations; mirrored spiral-out experiments including systematic patterning rotation to determine segment specific volume growth rates; experiments with a retracted and turned off gas injection system at different dwell times and varying loop numbers to differ between surface diffusion and gas flux related influences; finite difference simulations with extremely low diffusion coefficients; diffusion coefficient determination via numerical methods and correlated experiments; and video showing temporal coverage evolution. This material is available free of charge via the Internet at http://pubs.acs.org.

■ AUTHOR INFORMATION

Corresponding Author
*E-mail: harald.plank@felmi-zfe.at. Phone: +43 316 873 8821.
Notes
The authors declare no competing financial interest.

■ ACKNOWLEDGMENTS

■ REFERENCES

(1) *Nanofabrication Using Focused Ion and Electron Beams: Principles and Applications*; Utke, I., Moshkalev, S., Russell, P., Eds.; Oxford University Press: New York, 2012.
(2) Randolph, S. J.; Fowlkes, J. D.; Rack, P. D. *Crit. Rev. Solid State Mater. Sci.* 2006, 31, 55−89.
(3) van Dorp, W. F.; Hagen, C. W. *J. Appl. Phys.* 2008, 104, 081301−1−081301−42.
(4) (i) Donev, E. U.; Hastings, J. T. *Nanotechnology* 2009, 20, 505302. (ii) Donev, E. U.; Hastings, J. T. *Nano Lett.* 2009, 9, 2715−2718. (iii) Schardein, G.; Donev, E. U.; Hastings, J. T. *Nanotechnology* 2011, 22, 015301.
(5) Botman, A.; Mulders, J. J. L.; Hagen, C. W. *Nanotechnology* 2009, 20 (1), 372001.
(6) Smith, D. A.; Fowlkes, J. D.; Rack, P. D. *Nanotechnology* 2007, 18, 265308.
(7) Fowlkes, J. D.; Rack, P. D. *ACS Nano* 2010, 4, 1619−1629.
(8) Smith, D. A.; Fowlkes, J. D.; Rack, P. D. *Nanotechnology* 2008, 19, 415704.
(9) Smith, D. A.; Fowlkes, J. D.; Rack, P. D. *Small* 2008, 4, 1382−1389.
(10) Fowlkes, J. D.; Randolph, S. J.; Rack, P. D. *J. Vac. Sci. Technol., B* 2005, 23, 2825−2832.
(11) van Dorp, W.; Hansen, T. W.; Wagner, J. B.; De Hosson, J. T. B. *Beilstein J. Nanotechnol.* 2013, 4, 474−480.
(12) (i) van Dorp, W. F.; van Someren, B.; Hagen, C. W.; Kruit, P.; Crozier, P. A. *Nano Lett.* 2005, 5, 1303−1307. (ii) Bret, T.; Utke, I.; Hoffmann, P.; Abourida, M.; Doppelt, P. *Microelectron. Eng.* 2006, 83, 1482−1486. (iii) van Dorp, W. F.; Hagen, C. W.; Crozier, P. A.; van Someren, B.; Kruit, P. *Microelectron. Eng.* 2006, 83, 1468−1470. (iv) Córdoba, R.; Baturina, T. I.; Sesé, J.; Yu Mironov, A.; De Teresa, J. M.; Ibarra, M. R.; Nasimov, D. A.; Gutakovskii, A. K.; Latyshev, A. V.; Guillamón, I.; Suderow, H.; Vieira, S.; Baklanov, M. R.; Palacios, J. J.; Vinokur, V. M. *Nat. Commun.* 2013, 4, 1437. (v) van Dorp, W.; Zhang, X.; Feringa, B. L.; Hansen, T. W.; Wagner, J. B.; De Hosson, J. T. B. *ACS Nano* 2012, 6 (11), 10076−10081.
(13) (i) Perentes, A.; Bachmann, A.; Leutenegger, M.; Utke, I.; Sandu, C.; Hoffmann, P. *Microelectron. Eng.* 2004, 73−74, 412−416. (ii) Utke, I.; Jenke, M. G.; Iakovlev, V.; et al. *Nanoscale* 2011, 3 (7), 2718−2722.
(14) (i) Lassiter, M. G.; Liang, T.; Rack, P. D. *J. Vac. Sci. Technol., B* 2008, 26 (3), 963−967. (ii) Liang, T.; Frendberg, E.; Lieberman, B.; Stivers, A. *J. Vac. Sci. Technol., B* 2005, 23 (6), 31013105. (iii) Edinger, K.; Becht, H.; Bihr, J.; Boegli, V.; Budach, M.; Hofmann, T.; Koops, H. W. P.; Kuschnerus, P.; Oster, J.; Spies, P.; Weyrauch, B. *J. Vac. Sci. Technol., B* 2004, 22 (6), 2902−2906.
(15) Heerkens, C. T. H.; Kamerbeek, M. J.; van Dorp, W.; Hagen, C. W.; Hoekstra, J. *Microelectron. Eng.* 2009, 86, 961−964.
(16) Guan, Y.; Fowlkes, J. D.; Retterer, S. T.; Simpson, M. L.; Rack, P. D. *Nanotechnology* 2008, 19 (50), 505302.
(17) Jenke, M. G.; Lerose, D.; Niederberger, C.; Michler, J.; Christiansen, S.; Utke, I. *Nano Lett.* 2011, 11, 4213−4217.
(18) Mackus, A. J. M.; Mulders, J. J. L.; van de Sanden, M. C. M.; Kessels, W. M. M. *J. Appl. Phys.* 2010, 107 (11), 116102−1−116102−3.
(19) (i) Noh, J. H.; Nikiforov, M.; Kalinin, S. V.; Vertegel, A. A.; Rack, P. D. *Nanotechnology* 2010, 21 (36), 365302. (ii) (19) Roberts, N. A.; Noh, J. H.; Lassiter, M. G.; Guo, S.; Kalinin, S. V.; Rack, P. D. *Nanotechnology* 2012, 23 (14), 145301. (iii) Utke, I.; Hoffmann, P.; Berger, R.; Scandella, L. *Appl. Phys. Lett.* 2002, 80 (25), 47924794.
(20) Miura, N.; Ishii, H.; Shirakashi, J. I.; Yamada, A.; Konagai, M. *Appl. Surf. Sci.* 1997, 269−273, 113−114.
(21) (i) Fernandez-Pacheco, A.; De Teresa, J. M.; Cordoba, R.; Ibarra, M. R.; Petit, D.; Read, D. E.; O'Brien, L.; Lewis, E. R.; Zeng, H. T.; Cowburn, R. P. *Appl. Phys. Lett.* 2009, 94, 192509−1−192509−3. (ii) Serrano-Ramon, L.; Cordoba, R.; Rodriguez, L. A.; Magen, C.; Snoeck, E.; Gatel, C.; Serrano, I.; Ibarra, M. R.; De Teresa, J. M. *ACS Nano* 2001, 5 (10), 7781−7787. (iii) Gavagnin, M.; Wanzenboeck, H. D.; Belić, D.; Bertagnolli, E. *ACS Nano* 2013, 7 (1), 777−784. (iv) Gabureac, M.; Bernau, L.; Boero, G.; Utke, I. *IEEE Trans. Nanotechnol.* 2013, 12 (5), 668−673. (v) Gabureac, M.; Bernau, L.; Utke, I.; Boero, G. *Nanotechnology* 2010, 21, 115503.
(22) Huth, M.; Porrati, F.; Schwalb, C.; Winhold, M.; Sachser, R.; Dukic, M.; Adams, J.; Fantner, G. *Beilstein J. Nanotechnol.* 2012, 3, 597−619.
(23) Porrati, F.; Sachser, R.; Schwalb, C. H.; Frangakis, A. S.; Huth, M. *J. Appl. Phys.* 2011, 109, 0637151−1−063715−7.
(24) Kolb, F.; Schmoltner, K.; Huth, M.; Hohenau, A.; Krenn, J.; Klug, A.; List, E. J. W.; Plank, H. *Nanotechnology* 2013, 24, 305501.
(25) Utke, I.; Gölzhäuser, I. *Angew. Chem., Int. Ed.* 2010, 49, 9328−9330.
(26) Utke, I.; Friedli, V.; Purrucker, M.; Michler, J. *J. Vac. Sci. Technol., B* 2007, 25 (6), 2219−2223.
(27) Plank, H.; Gspan, C.; Dienstleder, M.; Kothleitner, G.; Hofer, F. *Nanotechnology* 2008, 19, 485302.
(28) Plank, H.; Haber, T.; Gspan, C.; Kothleitner, G.; Hofer, F. *Nanotechnology* 2013, 24, 1753605.
(29) Gabureac, M.; Bernau, L.; Utke, I. *J. Nanosci. Nanotechnol.* 2011, 11 (1−6), 7982−7987.
(30) Bernau, L.; Gabureac, M.; Erni, R.; Utke, I. *Angew. Chem., Int. Ed.* 2010, 49, 8880−8884.
(31) Cordoba, R.; Sese, J.; De Teresa, J. M.; Ibarra, M. R. *Microelectron. Eng.* 2010, 87 (5−8), 1550−1553.

2994

dx.doi.org/10.1021/am405591d | ACS Appl. Mater. Interfaces 2014, 6, 2987−2995

(32) Mulders, J. J. L.; Belova, L. M.; Riazanova, A. *Nanotechnology* **2011**, *22* (05), 055302.

(33) Langford, R. M.; Ozkaya, D.; Sheridan, J.; Chater, R. *Microsc. Microanal.* **2004**, *10*, 1122−1123.

(34) Miyazoe, H.; Utke, I.; et al. *J. Vac. Sci. Technol., B* **2010**, *28* (4), 744−750.

(35) Roberts, N. A.; Fowlkes, J. D.; Magel, G. A.; Rack, P. D. *Nanoscale* **2013**, *5* (1), 408−415.

(36) Roberts, N. A.; Magel, G. A.; Hartfield, C. D.; Moore, T. M.; Fowlkes, J. D.; Rack, P. D. *J. Vac. Sci. Technol., A* **2012**, *30* (4), 041404−041406.

(37) (i) Gopal, V.; Radilovic, V. R.; Daraio, C.; Jin, S.; Yang, P.; Stach, E. A. *Nano Lett.* **2004**, *4* (11), 2059−2063. (ii) Botman, A.; Mulders, J. J. L.; Weemaes, R.; Mentink, S. *Nanotechnology* **2006**, *17* (15), 3779−3785. (iii) Langford, R. M.; Wang, T. X.; Ozkaya, D. *Microelectron. Eng.* **2007**, *84* (5−8), 784−788.

(38) Mehendale, S.; Mulders, J. J. L.; Trompenaars, P. H. F. *Nanotechnology* **2013**, *24* (14), 145303.

(39) Porrati, F.; Sachser, R.; Schwalb, C. H.; Frangakis, A. S.; Huth, M. *J. Appl. Phys.* **2011**, *109* (06), 063715.

(40) Frabboni, S.; Gazzadi, G. C.; Felisari, L.; Spessot, A. *Appl. Phys. Lett.* **2006**, *88*, 213116-1−213116-3.

(41) Plank, H.; Noh, J. H.; Fowlkes, J. D.; Lewis, B.; Rack, P. D. *ACS Appl. Mater. Interfaces* **2014**, *6* (2), 1018−1024.

(42) Friedli, V.; Utke, I. *J. Phys. D: Appl. Phys.* **2009**, *42*, 125305.

(43) Bret, T.; Utke, I.; Hoffmann, P. *Microelectron. Eng.* **2005**, *78−79*, 307−313.

(44) DeMarco, A. J.; Melngailis, J. *J. Vac. Sci. Technol., B* **1999**, *17*, 3154−3157.

(45) Friedli, V. Focused electron- and ion-beam induced processes: in situ monitoring, analysis and modelling. Ph.D. Thesis, Ecole Polytechnique Féderale de Lausanne, 2008.

(46) Friedli, V.; Utke, I. http://www.empa.ch/GISsimulator; 2009.

(47) Plank, H.; Smith, D. A.; Haber, T.; Rack, P. D.; Hofer, F. *ACS Nano* **2012**, *6*, 286−294.